Open Plasma Science

Vol. ICPIG 2025, No. 3 (2026)

Special issue

History
Received December 16, 2025
Revised February 21, 2026
Accepted April 10, 2026
Published May 13, 2026

Identifiers
DOI 10.46298/ops.17125
HAL hal-05375995
ArXiv -
Zenodo -

Supplementary Material
-

Licence

©The Authors

Characterization of a plasma source for water treatment using electrical, optical, and chemical diagnostics

Maria Saba*[,1], Cristina Muja[1], Philippe Guillot[1], and Thomas Maho[1]

[1]Laboratoire Diagnostic des Plasmas Hors-Equilibre, Institut national universitaire Champollion, Université de Toulouse, Albi, France

Abstract

Hospital and urban wastewaters constitute major reservoirs of multidrug-resistant bacteria (MRB), antibiotic resistance genes (ARGs), and persistent pharmaceutical contaminants, which are only partially removed by conventional treatment plants. As a result, these pollutants are still detected in treated effluents that are discharged into the environment or reused, which raises serious public health concerns – especially in the context of agricultural irrigation. This study explores a novel immersed dielectric barrier discharge (DBD) plasma source engineered for point-of-use decontamination of wastewater at emission sites. The plasma device was thoroughly characterized by electrical, optical, and chemical diagnostics to elucidate its operating regimes and capacity to generate reactive oxygen and nitrogen species (RONS) at the plasma–liquid interface. Findings demonstrate that the composition of the carrier gas strongly influences the production and transfer of short- and long-lived oxidants into the liquid phase. These results provide quantitative insights that support the ongoing optimization of plasma-based advanced oxidation processes (AOPs) systems for decentralized water treatment. They further illustrate how tuning the discharge operating conditions and carrier-gas admixtures can be used to enhance the formation and transfer of oxidants into the liquid phase, contributing to the broader field of plasma-liquid applications for the mitigation of emerging contaminants.

Keywords— gas-liquid interface plasma, electrical diagnostics, imaging, optical emission spectroscopy, reactive species

* Corresponding author: maria.saba@univ-jfc.fr

Cite as: Saba *et al.*, Characterization of a plasma source for water treatment using electrical, optical, and chemical diagnostics, *Open Plasma Science* ICPIG 2025, 3 (2026), doi: 10.46298/ops.17125

Contents

1 Introduction

Hospital, laboratory, and urban wastewater represent major vectors for both microbiological and chemical contamination. These effluents contain a wide range of microorganisms, including pathogens, together with pharmaceutical residues and antibiotics. Such compounds exert a selective pressure on microbial populations, promoting the emergence and dissemination of multidrug-resistant bacteria (MRB) and antibiotic resistance genes (ARGs). Their increasing presence in the environment now constitutes a significant public health concern [MLK20].

Conventional wastewater treatment plants (WWTPs) efficiently reduce organic matter and nutrient loads but are not specifically designed to eliminate MRB or degrade persistent pharmaceutical compounds [SSSM22]. Several studies have shown that the biological and chemical conditions prevailing in these facilities—high microbial density, biofilm development, and sub-inhibitory antibiotic concentrations—can, conversely, facilitate the horizontal transfer of resistance genes [NMMR+25]. Consequently, treated effluents released into receiving environments often still contain resistant microorganisms and micropollutants that can contaminate soils and surface waters. This issue is further aggravated by the increasing adoption of the REUSE concept, which promotes the reuse of treated wastewater for agricultural irrigation or industrial processes in response to water scarcity and climate change [TBB24]. While this practice offers ecological and economic advantages, numerous studies have reported the persistence of pathogenic microorganisms and MRB in reclaimed water, raising concerns regarding soil, plant, and food-chain contamination [PZDdlSBC+17, CAB+17]. Managing this challenge requires the development of decentralized or complementary treatments capable of reducing both microbial and chemical loads upstream of existing sanitation systems [SN23].

In this context, cold atmospheric plasma (CAP) technology has attracted attention as a promising advanced oxidation and antimicrobial process [CMM+22]. CAP operated in noble or molecular gases (e.g., He, Ar, air, N_2, O_2 and mixtures thereof) generate in gas-phase a rich mixture of reactive oxygen and nitrogen species (RONS) through electron-molecule collisions and subsequent reaction cascades involving the feed gas,

ambient air, and water vapour. A fraction of these gas-phase species, together with radicals formed directly at the plasma–liquid interface, is transferred into the aqueous phase, and gives rise to a population of oxidants (e.g. H_2O_2, NO_2^-, NO_3^-, O_2^-, ...) known for their strong oxidative and biocidal properties [BKL+16]. Through simultaneous physical effects (electron impacts, UV radiation, electric fields) and chemical reactions (radical formation, oxidation cascades), plasma–liquid systems can achieve inactivation of microorganisms and degradation of organic contaminants [GBB+21, TSC+23].

Among the various plasma configurations investigated, Dielectric Barrier Discharges (DBDs) are among the most prominent for producing non-thermal plasma at atmospheric pressure owing to their stability, controllability, and suitability for liquid-phase applications [LMZ+19]. In water treatment, different plasma–liquid coupling modes have been developed according to the location of the discharge relative to the liquid [ZNTK+20]. In the indirect mode, the plasma is generated *above the liquid surface*. The gas-phase species are transported towards the plasma-liquid interface by the gas flow and diffusion, where part of them is converted into aqueous oxidants via interfacial reactions and dissolution [BKL+16]. This approach allows better control of gas composition and discharge uniformity but is limited by the diffusion of RONS across the gas–liquid interface [CMM+21]. In contrast, the direct or immersed mode involves plasma formation *within the liquid*, either through microdischarges or within gas bubbles injected into the medium [LWZ+22]. This setup enhances plasma–liquid coupling, leading to higher production and transfer rates of short- and long-lived reactive species, improving both oxidation and microbial inactivation efficiency. Hybrid designs combining both modes have also been reported, maximizing interfacial area and plasma exposure to better address complex aqueous matrices [GBB+21].

Building on this context, the present study was designed to develop and thoroughly characterize an immersed bubble dielectric barrier discharge (DBD) plasma source, in which a dielectric tube injects a continuous stream of gas into the liquid so that microdischarges ignite both inside the tube and in the gas cavity at its outlet, i.e., directly within the liquid volume, with a specific focus on its optimization for local wastewater treatment, particularly near emission points such as hospital sinks or laboratory drains. The research aimed first to achieve a rigorous electrical characterization of the plasma source by quantifying discharge power, energy transfer efficiency, and their dependence on key operating parameters. Next, the study sought to elucidate the spatiotemporal dynamics of the discharge using fast optical diagnostics, providing insight into the ignition, propagation, and extinction processes occurring within the reactor and at the plasma–liquid interface. A further objective was to identify and quantify the reactive species generated in both the plasma phase and the liquid, employing optical emission spectroscopy and chemical assays to reveal how gas composition modulates interfacial plasma chemistry. Finally, the work integrated electrical, imaging, and chemical diagnostic data to establish the principal mechanisms by which reactive oxygen and nitrogen species (RONS) are formed and transferred into the aqueous phase. This multidisciplinary approach advances both the fundamental understanding and the practical control of plasma–liquid interactions, supporting the development of robust and scalable plasma-based technologies for on-site wastewater decontamination.

2 Materials and Methods

2.1 Experimental set-up

The plasma reactor used in this study belongs to the class of bubble discharge dielectric barrier discharge (DBD) reactors [VNL16], specifically designed to produce plasma directly within the liquid phase through gas injection. The system consists of two main components, both made of 1.6 mm-thick borosilicate glass: the liquid container and the reactor head.

The container, which holds the liquid to be treated, is cylindrical, with a diameter of 3.3 cm and a height of 7.4 cm. In this study, 47 mL of type I ultra-pure water (Direct-Q UV, Millipore) was used as the working

liquid. The water was not degassed prior to treatment. The head consists of a 15 cm-long tube with an inner diameter of 4 mm, embedded in an arched structure containing two parallel gas outlet ports.

One extremity of the tube is immersed into the liquid, while the arched structure acts as the reactor lid and mechanical support. The feed gas is introduced through an inlet located at the upper part of the arched section, flows through the internal tube, and exits from its open, submerged end. This configuration produces a continuous stream of gas bubbles in the liquid, enabling the *in situ* formation of microdischarges at the gas–liquid interface.

Four gas bottles provided by Linde company were employed to investigate the effect of gas chemistry on discharge behavior and reactive species formation: He, He–0.2% O_2, He–0.2% N_2, and He–0.2% air. Gas bottles (Helium 5.0 – 99,999% purity, Azote 4.5 – 99,995% purity, Synthetic air 5.0 – 99,999% purity and special gas-mixture for He-O_2) were provided by Linde company. The gas flow rate was maintained at 2 L.min^{-1} using a mass-flow controller (EL-FLOW Select, model F-201CV, Bronkhorst B.V.).

The high-voltage electrode is a metallic rod, 1 mm thick, inserted into the tube until its tip reaches the end. The grounded electrode is wrapped spirally around the container. The figure 1A shows the schematic diagram of the plasma source.

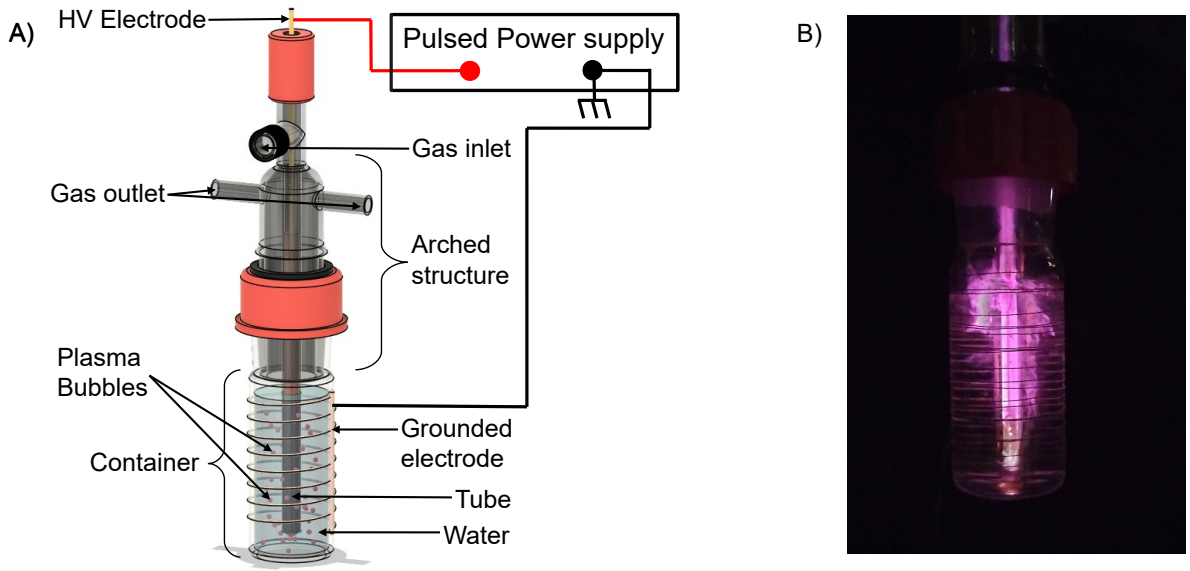

Figure 1: (A) Schematic diagram of the plasma source. (B) Photograph of the plasma source using pure helium as the carrier gas.

Both electrodes are connected to a pulsed power supply developed at the GREMI Laboratory (Orléans, France), which delivers fixed pulses of 4 µs duration. The applied voltage can be varied from 0 to 20 kV, with a frequency adjustable between 1 and 30 kHz. For this study, the operational frequency was set at 20 kHz.

When the high voltage is applied, microdischarges ignite inside the glass tube and within the gas cavity formed at its outlet, establishing an active plasma region that interacts directly with the surrounding liquid medium. This configuration combines the advantages of dielectric confinement with direct plasma–liquid contact, enabling efficient generation and transfer of reactive oxygen and nitrogen species essential for water decontamination.

2.2 Electrical diagnostics

The electrical characterization of the plasma reactor was performed using the equivalent electrical circuit (EEC) approach, which models the plasma source as an electrical circuit that reflects its electrical properties.

This method, widely applied to dielectric barrier discharge (DBD) systems [PB19, PGK+11, LLKA04, LN03] and other plasma configurations [CER99, SGA+20], provides a simplified yet accurate framework for determining internal discharge parameters that cannot be directly measured.

In the EEC model, the dielectric barriers and the gas gap are represented by capacitors, while the plasma channel is described as a resistor connected in parallel with the gas-gap capacitance. The resistor accounts for the conductive phase of the discharge, during which microdischarges locally bridge the electrodes. By solving the circuit equations using experimental voltage and current waveforms, it is possible to extract key internal quantities such as the discharge current and the voltage drop across the gas gap. These values were subsequently used to calculate the power dissipated in the plasma and to analyze the energy coupling efficiency of the reactor.

The applied voltage (V) was recorded using a high-voltage probe (Tektronix P6015A), and the total current (I) was measured with a Pearson Current Monitor (Model 6585). Both signals were simultaneously captured with a digital oscilloscope (Rohde & Schwarz RTE1204). (see figure 2).

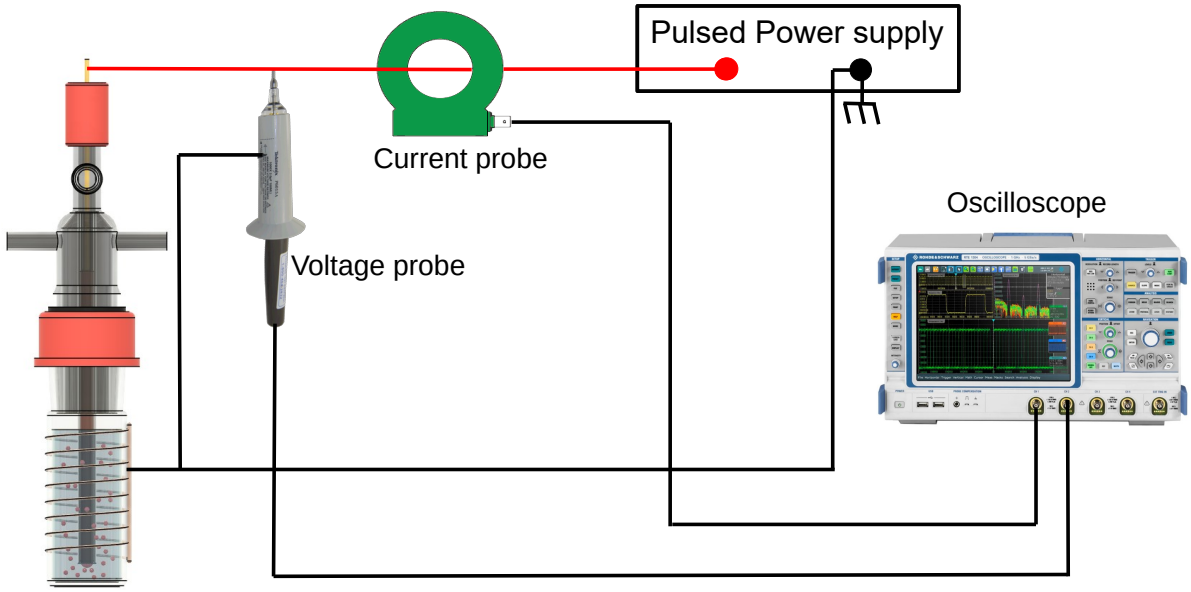

Figure 2: Experimental setup for electrical measurements

The Q–V plot (Lissajous curve) of an ideal dielectric barrier discharge (DBD) reactor operating under a sinusoidal voltage allows the capacitances of the reactor components to be determined graphically [PHK+12]. To experimentally determine the capacitances of our reactor, its Q–V plot was obtained while operating under a sinusoidal voltage. The sinusoidal mode was used exclusively for the Q–V plot analysis in order to mimic the ideal case of a sinusoidally driven DBD reactor, whereas all other studies in this work were performed using the initial high-voltage pulsed generator.

To obtain the Q–V plot, the reactor was connected in series with a known measurement capacitor (Jennings UCSL-1000-3S, set to C_m = 100pF) (see Figure 3A). A sinusoidal voltage was applied to the system using a high-voltage AC power supply (Spitzenberger & Spies EV-1200/FS) operating at 20 kHz. The applied voltage waveform is shown in Figure 3B. Both the applied voltage and the voltage across the measurement capacitor were monitored using two identical Tektronix P6015A probes and recorded simultaneously with the same oscilloscope.

The charge transferred through the circuit, $Q_m = C_m \times V_m$, was plotted as a function of the applied voltage V(t), generating a Q–V plot characteristic of the reactor. The slope of each linear segment provided

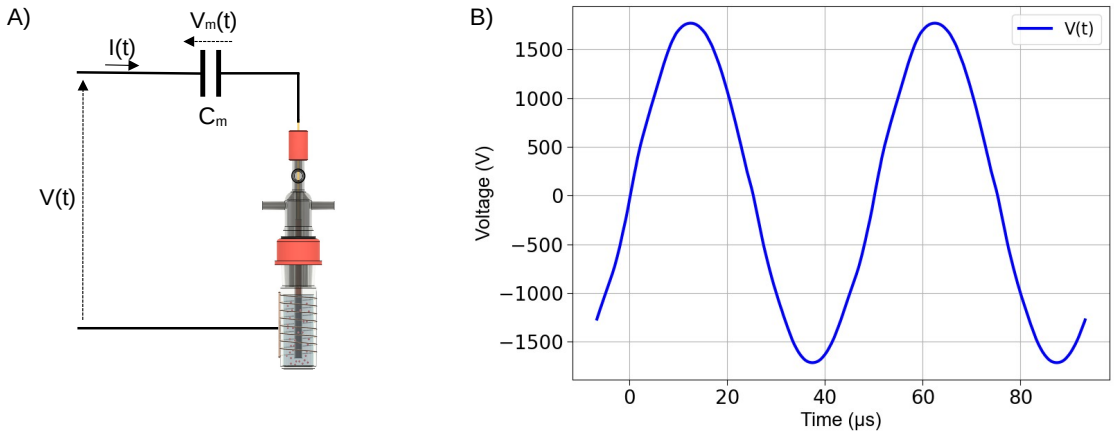

Figure 3: (A) Experimental setup for plotting the Lissajous curve. V(t) is the applied voltage, I(t) is the total current, C_m is the capacitance of the measurement capacitor, and $V_m(t)$ is the voltage across the measurement capacitor. (B) Sinusoidal applied voltage waveform used exclusively for the Q-V plot analysis, with an RMS value of 1200 V and a frequency of 20 kHz.

the equivalent capacitances associated with the dielectric and gas regions.

This analysis allowed the determination of the intrinsic electrical parameters of the plasma source and provided a quantitative basis for correlating discharge behavior with operating conditions, a methodology commonly used for the characterization of microdischarge-driven DBD systems.

2.3 Optical diagnostics

2.3.1 Camera imaging

The spatio-temporal evolution of the discharge inside the reactor during a single high-voltage pulse was investigated using an intensified charge-coupled device (ICCD) camera (Princeton Instruments PI-MAX-1). The emitted light was collected through a UV-grade objective (Nikon Nikkor 80–400 mm) equipped with an extension ring to ensure optimal focusing on the discharge region. The ICCD camera was synchronized with the applied voltage pulse through an external trigger to capture time-resolved images. Each image was acquired with a gate width of 10 ns, corresponding to a temporal resolution sufficient to resolve individual stages of the microdischarge development. To improve the signal-to-noise ratio, each frame represents the cumulative average of 1000 gated exposures.

2.3.2 Optical Emission Spectroscopy

Plasma spectral characterization was performed by optical emission spectroscopy (OES) to identify reactive species generated under different gas compositions (He, He–0.2% O_2, He–0.2% N_2, and He–0.2% air). Emission spectra were recorded using a spectrometer (Princeton Instruments SpectraPro HRS-750) coupled to an ICCD detector (Princeton Instruments PI-MAX-4). Plasma emission was transmitted to the spectrometer via a 600 μm-core, 2 m-long optical fiber (Ocean Optics). Spectra were acquired over a wavelength range of 200–900 nm with an integration time of 1 ms. Wavelength calibration was performed using the IntelliCal system provided with the spectrometer, and relative intensity calibration was performed using a deuterium halogen reference lamp (Ocean Optics DH2000).

Two distinct configurations were employed for each gas mixture (Figure 4). In the first configuration, the optical fiber was placed at position 1 to collect light from the plasma formed inside the tube. In the second

configuration (Position 2), the fiber was positioned below the reactor, facing the gas cavity at the tube outlet, to capture the emission from the plasma–liquid interface. During this second measurement, the tube was covered with black tape to suppress any optical contribution from the plasma inside the tube, ensuring that only light from the interfacial region was recorded.

Each emission spectrum was acquired in triplicate to ensure reproducibility, and the final spectra reported in this work correspond to the averaged results. This combined imaging and spectroscopic analysis provided complementary insights into the discharge propagation dynamics and the formation pathways of reactive species within the plasma and at the plasma–liquid interface, critical for understanding the mechanisms of plasma-assisted water treatment.

2.4 Chemical diagnostics

Preliminary chemical diagnostics were performed using the potassium iodide–starch (KI–starch) indicator method, a qualitative and semi-quantitative technique commonly applied to visualize reactive oxygen species (ROS) generated in plasma-treated water [SSK23, MKNK20]. This method enables the indirect detection of strong oxidants such as ozone (O_3), hydroxyl radical (OH) and hydrogen peroxide (H_2O_2), based on their ability to oxidize iodide ions.

In this system, iodide ions (I^-) are oxidized by reactive species with an oxidation potential higher than that of molecular iodine ($E^\circ = 0.54$V), leading to the formation of iodine (I_2). The produced I_2 then reacts with excess iodide to form triiodide (I_3^-), which further forms a stable blue–black complex with starch [BLU+22]. The intensity of this complex, characterized by a strong absorption peak near 600 nm, reflects the abundance of oxidizing species in the treated solution.

A 500 mL KI–starch stock solution was prepared by dissolving 5 g of soluble starch and 3 g of potassium iodide (KI) in ultrapure water under gentle heating to ensure complete dissolution. Following plasma treatment, equal volumes of the treated water and KI–starch solution were mixed at a 1:1 ratio and allowed to react for 40 minutes at ambient temperature to ensure reaction completeness. The mixture was then transferred into well plates for spectrophotometric analysis, and the absorbance was measured at 600 nm using a multimode microplate reader (BioTek Synergy H1). The measured absorbance serves as an indicator of the total concentration of RONS accumulated in the plasma-treated water.

This diagnostic was conducted for the four carrier gas compositions—He, He–0.2% O_2, He–0.2% N_2, and He–0.2% air—to assess how gas composition influences the oxidative strength of the plasma. Each measurement was performed in triplicate, and the results were averaged to ensure reproducibility and minimize systematic variability.

3 Results and Discussion

3.1 Power dissipated in the plasma discharge

Although the geometric configuration of the plasma reactor is relatively complex, a cross-sectional view taken through the center of the container (see Figure 5A) shows that the system can be approximated as a coaxial dielectric barrier discharge (DBD). In this representation, the glass tube, the water layer, and the outer glass container jointly constitute the dielectric barriers surrounding the plasma region.

Ultrapure water, characterized by its very low electrical conductivity (0.055 $\mu S.cm^{-1}$ at 25 °C) and high relative permittivity ($\epsilon_r \approx 80$ at room temperature), behaves as an effective dielectric under these conditions [SW21, YJY+18]. However, when exposed to plasma, chemical reactions at the plasma–liquid interface generate reactive oxygen and nitrogen species (RONS), which progressively increase the ionic conductivity of the liquid. Accordingly, all electrical measurements presented in this section were conducted at the initial stage

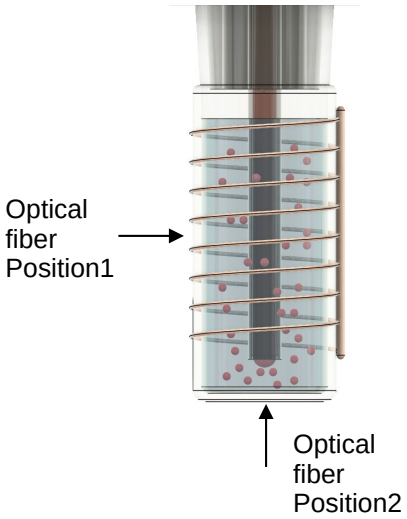

Figure 4: Schematic showing the position of the optical fiber for the two OES measurements.

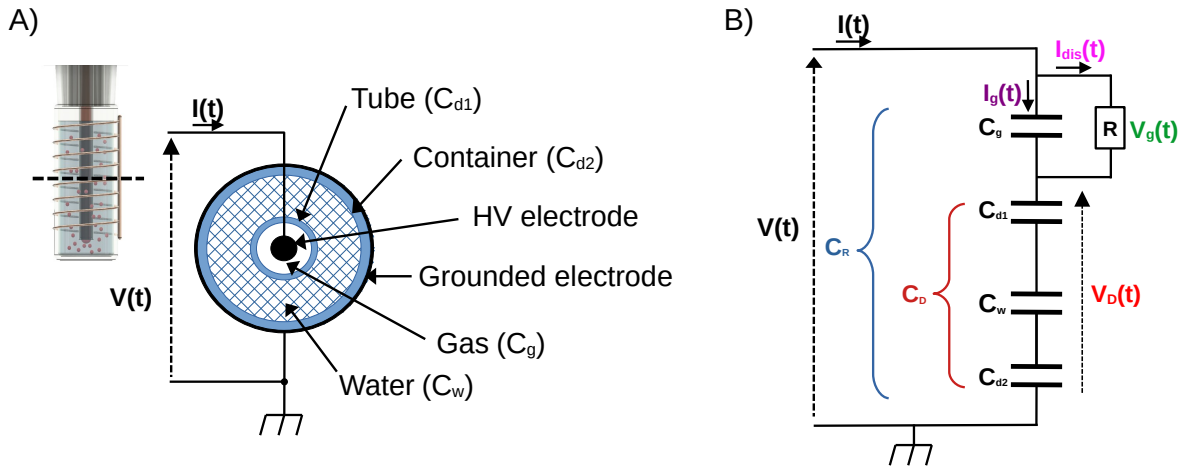

Figure 5: (A) Cross section of the plasma reactor. (B) Equivalent electrical circuit of the plasma source.

of plasma operation, when only minimal concentrations of reactive species had accumulated. Under these conditions, the water can still be reasonably treated as a dielectric layer in the analytical model [VNBL18].

The equivalent electrical circuit (EEC) used to describe the reactor behavior is presented in figure 5B. The model follows those typically applied to conventional coaxial DBD systems. The capacitive elements C_g, C_{d1}, C_w and C_{d2} represent the equivalent capacitances of the gas gap (inside the tube), the inner dielectric barrier (tube wall), the water layer, and the external container wall, respectively.

The applied voltage is denoted by V(t), and the total current through the circuit by I(t). The discharge current I_{dis} (t) represents conduction through the microdischarges, while I_g (t) corresponds to the displacement current across the gas gap. The voltages across the gas region and dielectric barriers are represented by V_g (t) and V_D (t), respectively.

The total capacitance of the dielectric barrier C_D is given by the following equation:

$$C_D = \left[\frac{1}{C_{d1}} + \frac{1}{C_w} + \frac{1}{C_{d2}}\right]^{-1} \tag{1}$$

The total capacitance of the reactor C_R is expressed as:

$$C_R = \left[\frac{1}{C_D} + \frac{1}{C_g}\right]^{-1} \tag{2}$$

By applying Kirchhoff's law to the equivalent electrical circuit, the instantaneous voltage across the gas gap and the discharge current can be expressed as functions of the applied voltage V(t) and the total measured current I(t):

$$V_g(t) = V(t) - \frac{1}{C_D}\int_0^T I(t)\,dt \tag{3}$$

$$I_{dis}(t) = I(t) - C_g\frac{dV_g(t)}{dt} \tag{4}$$

The total power delivered by the power supply, P_{tot}, and the power dissipated in the discharge, P_{dis}, are given by the following equations:

$$P_{tot}(t) = I(t) \times V(t) \tag{5}$$

$$P_{dis}(t) = I_{dis}(t) \times V_g(t) \tag{6}$$

The instantaneous total energy delivered by the power supply, E_{tot} (t), and the energy dissipated in the discharge, E_{dis} (t), are given by the following equations:

$$E_{tot}(t) = \int_0^t P_{tot}(\tau)\,d\tau \tag{7}$$

$$E_{dis}(t) = \int_0^t P_{dis}(\tau)\,d\tau \tag{8}$$

To solve equations (3) and (4), the capacitances C_D and C_g were first determined experimentally. A typical Q–V (Lissajous) plot for an ideal sinusoidally driven DBD exhibits a parallelogram shape as shown in Figure 6A. The slope of the branches (AB and DC) equals the total capacitance of the reactor, whereas the slope of the branches (BC and AD) equals the capacitance of the dielectric barrier. The Q–V plot obtained for our reactor under sinusoidal excitation, shown in Figure 6B, displays a similar quasi-parallelogram geometry, confirming that the plasma reactor can be suitably approximated as a coaxial DBD.

The Q–V plot obtained for our reactor under sinusoidal excitation, shown in Figure 6B, displays a quasi-parallelogram geometry, confirming that the plasma reactor can be suitably approximated as a coaxial DBD. Since the experimental figure was slightly distorted, the parallelogram was graphically reconstructed in order to match the ideal sinusoidally operated DBD case. The slopes of the reconstructed sides were then graphically determined to deduce the capacitances. From this analysis, the equivalent capacitances were determined as C_R = 4.08 $\pm$ 0.19 pF, C_D = 21.43 $\pm$ 0.40 pF, and C_g = 4.71 $\pm$ 0.27 pF. The value of C_g was obtained by rearranging Equation 2.

For comparison, the theoretical capacitances were calculated using the expression for a coaxial dielectric layer:

$$C = \frac{2\pi\epsilon_0\epsilon_r L}{ln(r_1/r_2)} \tag{9}$$

where ϵ_0 is the vacuum permittivity, ϵ_r the relative permittivity of the dielectric material, L the axial length of the dielectric layer, r_1 and r_2 the inner and outer radius, respectively.

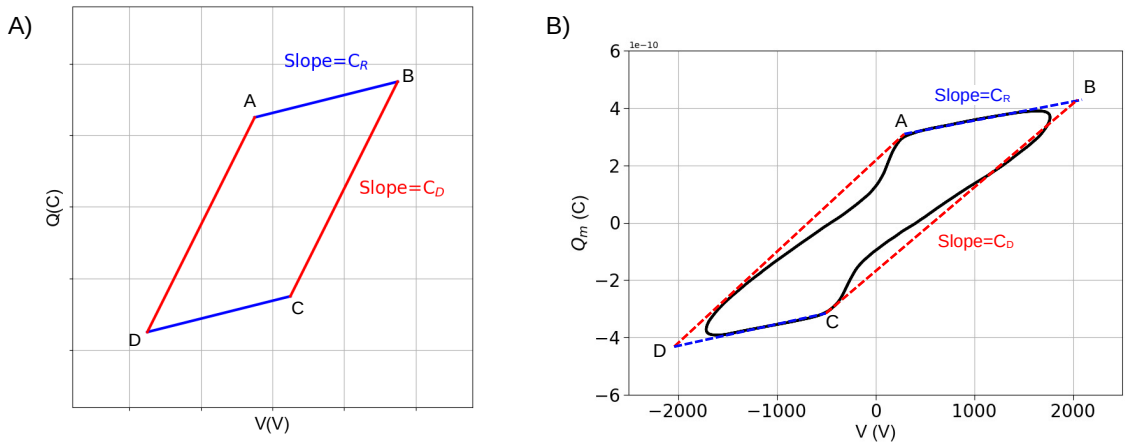

Figure 6: (A) Typical Q–V plot for an ideal sinusoidally operated DBD reactor. (B) Q–V plot of our plasma reactor operating under sinusoidal excitation. The dashed lines represent the reconstructed parallelogram.

Applying equation (9) to the reactor geometry yields the following theoretical values : C_g=6.5 pF, C_{d1}=34.7 pF, C_w=140 pF and C_{d2}=239.2 pF. By substituting these values into equations (1) and (2), we obtain the equivalent capacitances C_D = 25.63 pF and C_R = 5.18 pF. The experimental and theoretical results agree within approximately 15–30%, consistent with expected deviations arising from the simplified coaxial approximation of the reactor geometry.

Once the equivalent capacitances are determined, we can now analyse our pulsed driven reactor using the equivalent circuit. Figure 7A presents the measured waveforms of the applied voltage V(t) and total current I(t). The carrier gas used was helium, and the reactor contained 47 mL of ultrapure water. Although the pulsed power supply was set to 15 kV at 20 kHz, the actual voltage amplitude applied to the reactor was 6.7 kV. The voltage waveform consists of a symmetrical main pulse, with both the rising (A to B) and falling edges (B to C) lasting 2 µs. Following the main pulse, the voltage slightly changes polarity of about −1.2 kV (D) and then exhibits damped oscillations for approximately 20 µs before returning to zero. These oscillations are attributed to the resonant response of the power-supply–reactor system: after the main pulse, the residual energy stored in the generator and in the reactor capacitances is exchanged with the inductive elements of the circuit, leading to a transient ringing. This reactive energy is progressively dissipated by resistive losses in the circuitry and in the plasma-reactor assembly, so that both the voltage and current eventually decay to zero [PKBH12].

The current waveform shows an initial discharge of approximately 0.1 A associated with the rising edge of the voltage pulse (A to C), followed by a second, negative discharge of about −0.07 A associated with the falling edge C to E. Slightly before returning to zero, the current undergoes a rapid oscillation and then returns slowly to zero (E to F). This coincides with the polarity reversal of the voltage.

I_{dis}(t) and V_g(t) were derived by solving equations (3) and (4) using the experimental data obtained during V(t) and I(t) measurements. Figure 7B shows the resulting waveforms. The discharge current exhibits a waveform similar to the total current but with a slightly lower amplitude of approximately 0.096 A (B), due to the removal of the displacement current from the total current. V_g(t) starts to rise with the total voltage, but at 1.6 kV it starts to drop (B). In fact, the first discharge charges the dielectric capacitance C_D through accumulating charges on the surface of the dielectric barrier. This creates an electric field that opposes the externally applied electric field, which causes the voltage drop across the gas gap (B to C) [LN01]. Then V_g(t) rises again with opposite polarity, which causes the second discharge (C to D).

Figure 7C presents both the instantaneous total power delivered by the power supply and the power

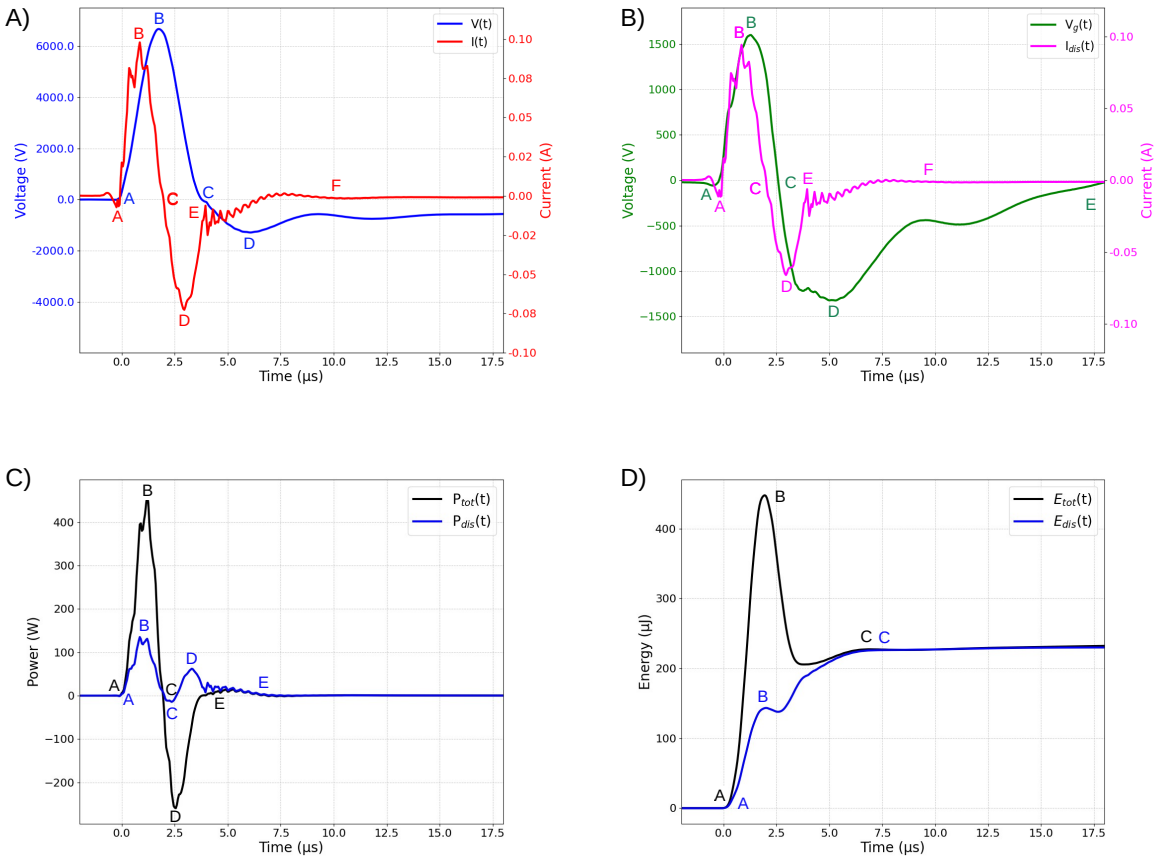

Figure 7: Electrical diagnostics of the plasma source operated with pure helium as the carrier gas (2 L·min^{-1}) and 47 mL of ultrapure water inside the container. The voltage indicated on the power supply was 15 kV at 20 kHz. (A) In blue, the measured waveform of the applied voltage; in red, the waveform of the total current. (B) In green, the voltage across the gas gap; in magenta, the discharge current, both obtained from the equivalent electrical circuit model. (C) In black, the instantaneous total power delivered by the power supply; in blue, the instantaneous power dissipated in the plasma. (D) In black, the instantaneous total energy delivered by the power supply; in blue, the instantaneous energy dissipated in the plasma. The total energy dissipated in the plasma during one pulse is 448.1 µJ.

dissipated in the plasma, calculated using equations (5) and (6). These curves reveal two distinct discharge events. During the first event, the total power $P_{tot}(t)$ is positive, indicating active energy injection into the system, while a fraction of this power is dissipated in the plasma as $P_{dis}(t)$. During the second discharge, $P_{tot}(t)$ becomes negative, indicating that part of the energy previously stored in the reactor and in the dielectric capacitances is fed back to the power supply : the residual charge on the dielectric is released and used to sustain the discharge without additional net input from the source. The corresponding evolution of the cumulative energies in Figure 7D illustrates this exchange between the energy initially delivered by the supply and the energy ultimately dissipated in the plasma.

Figure 7D shows the time evolution of the total energy delivered by the power supply and the energy dissipated in the plasma, calculated using equations (7) and (8). The first rise of the $E_{dis}(t)$ curve correspond to the energy dissipated in the first discharge (A to B), which is equal to 144 µJ, while the second rise corresponds to the energy dissipated in the subsequent discharge, 83.8 µJ , obtained by subtracting the first contribution from the total energy dissipated during the pulse (B to C). The $E_{tot}(t)$ curve, representing the cumulative

energy delivered by the supply, exhibits a single rise during the first discharge, reaching 448.1 µJ (A to B). Part of this energy is directly dissipated in the first discharge, while another part is temporarily stored in the reactor and dielectric capacitances through charge accumulation [RHZ+23]. The stored charge is then released and sustains the second discharge without additional net input from the power supply, in agreement with the negative values of P_{tot}(t) observed in Figure 7C [PKBH12].

At the end of the excitation, E_{dis}(t) and E_{tot}(t) converge around 227.8 µJ (C). This outcome reflects the boundary of the model, which incorporate only plasma dissipation and neglects losses due to the dielectric or electromagnetic radiation. Thus, the final value depicts the net energy transferred to the plasma after both discharge events are completed.

3.1.1 Spatiotemporal plasma evolution

Figure 8 presents time-resolved ICCD images acquired at successive delay times during a single voltage pulse. The experiments were performed with pure helium as the carrier gas at a flow rate of 2 L·min^{-1}, using 47 mL of ultrapure water as the working liquid. The applied voltage was set to 15 kV with a pulse frequency of 20 kHz. These images provides insight into the spatiotemporal evolution of the plasma inside the reactor during a voltage pulse. The positions of the tube and container walls, not directly visible in the raw images, are outlined with dashed white lines for reference.

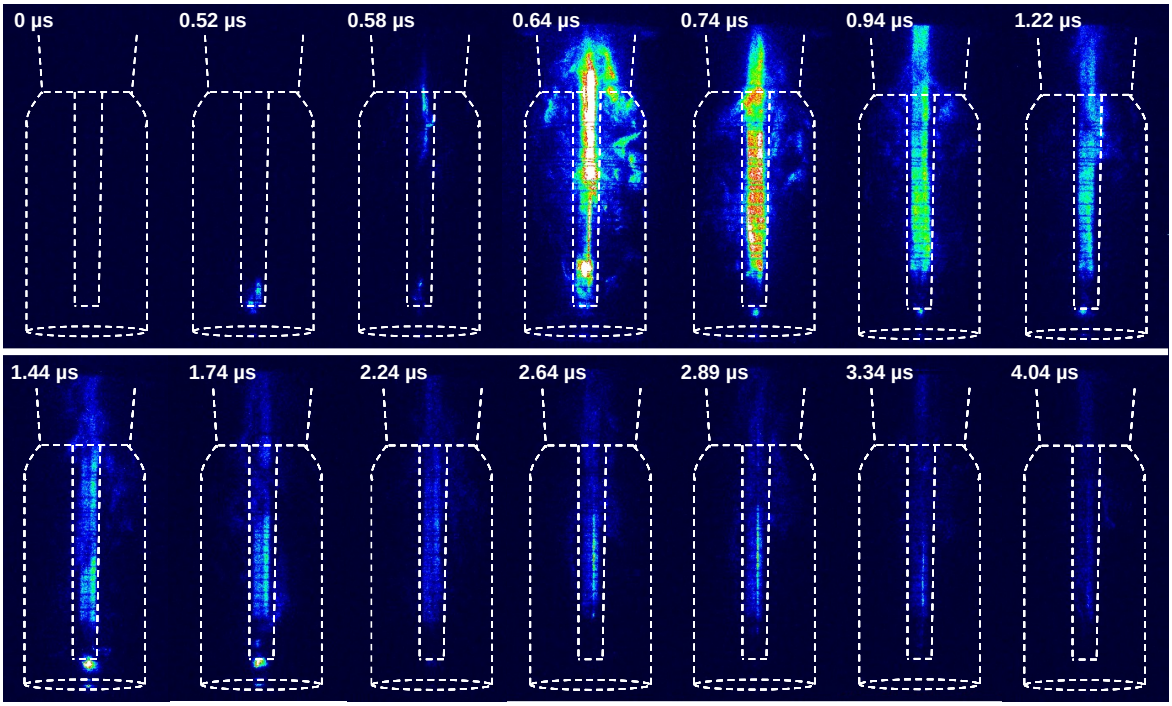

Figure 8: Spatiotemporal evolution of the plasma inside the reactor. The carrier gas is pure helium, flowing at 2 L·min^{-1}. The voltage indicated on the power supply is 15 kV at 20 kHz. The container holds 47 mL of ultrapure water. The tube and container boundaries are marked by white dashed lines. The time shown in the top left of each image corresponds to the time elapsed since the beginning of the pulse.

The first visible plasma emission appears at 0.52 µs after the beginning of the pulse and is localized at the tip of the high-voltage electrode. This observation suggests that electric field enhancement at the electrode tip leads to the initial breakdown, which is typical of DBD reactors with pin-to-liquid or pin-to-dielectric geometries [BKK+21]. This emission is shortly followed by the formation of an ionization front (0.58–0.64

µs), emerging from the upper region of the tube and propagating rapidly downward along the glass wall. This fast streamer propagation is sustained by the applied voltage and the helium atmosphere.

By 0.74 µs, the plasma column extends over nearly the full length of the tube and is characterized by intense emission, with the maximum intensity observed in the central region. The absence of emission near the tube outlet is likely due to an increase of local humidity and vapor-phase water content, which raise the breakdown threshold and locally suppress plasma formation. From 0.94 to 1.44 µs, the plasma emission inside the tube becomes more uniform, suggesting a transition from initial streamer channels to a more diffuse glow-like discharge [ZYW+19]. This observation indicates that a significant fraction of the deposited energy is, at this stage, being transferred towards the gas cavity and plasma–liquid interface region. Between 1.74 and 2.64 µs, the emission intensity gradually decreases, indicating plasma decay as the applied voltage drops and less energy is delivered to the discharge.

A secondary, weaker emission appears inside the tube at 2.64 µs, corresponding to the residual discharge discussed in the previous section. Complete plasma extinction occurs after approximately 4.04 µs, consistent with the trailing edge of the voltage pulse and the dissipation of residual surface or space charges.

Simultaneously, starting at around 0.74 µs, a luminous region appears at the tube outlet and within the gas cavity formed in the water. This region reaches peak intensity at 1.44 µs, in phase with glow discharge development inside the tube, then declines and vanishes by 2 µs. This secondary discharge is attributed to field focusing at the interface and the enhanced conductivity of the vapor cavity, which facilitates charge transfer from the plasma in the tube to the water or bubble interface [SFBK11].

In some images, faint light is observed outside the tube, within the water container volume. These emission do not originate from discharges occurring inside the gas bubbles but are due to optical reflections and scattering of the intense plasma emission produced inside the tube. The presence and intensity of this scattered light are influenced by the distribution and dynamics of the bubbles in the liquid phase.

3.1.2 Reactive species generated in the gas phase

Figure 9A shows the optical emission spectrum (OES) measured inside the discharge tube (position 1), while Figure 9B presents the OES at the gas–liquid interface (position 2). In both cases, the carrier gas is pure helium (2 L·min^{-1}), the applied voltage is 15 kV at 20 kHz, and the liquid phase consists of 47 mL ultrapure water.

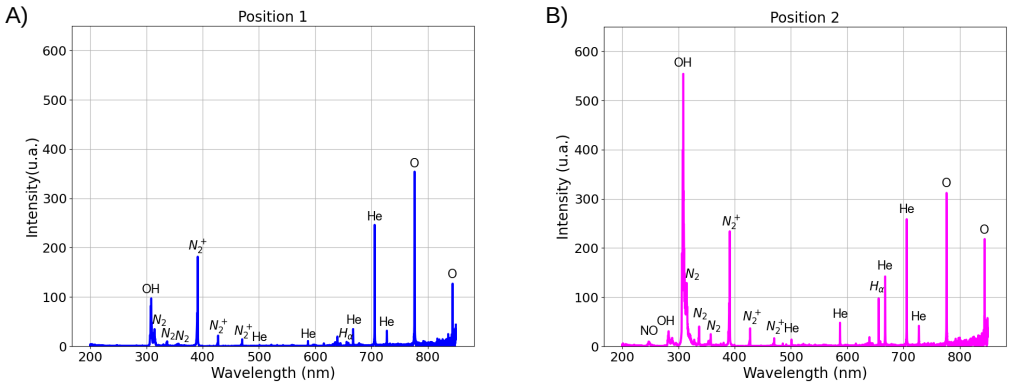

Figure 9: The carrier gas is pure helium flowing at 2 L·min^{-1}. The voltage indicated on the power supply is 15 kV at 20 kHz. The container holds 47 mL of ultrapure water. (A) Calibrated spectrum taken at position 1, corresponding to the plasma inside the tube. (B) Calibrated spectrum taken at position 2, corresponding to the plasma–water interface.

For both measurement positions, the emitted photons must follow the same optical path—through water and borosilicate glass—before being collected by the optical fiber. Consequently, transmission below about

280-300 nm is strongly reduced by absorption, resulting in a very low apparent intensity in this spectral range for both positions. Yet, a key distinction emerges: at position 2 (plasma–liquid interface), a discernible NO(A–X)(0–0) emission band is observed at 247 nm, whereas it is absent at position 1 (inside the tube). This result suggests that the appearance of NO emission at the interface is not a consequence of differential absorption, but reflects a true chemical difference: the formation of NO occurs much more efficiently at the plasma–liquid boundary than within the dry plasma core [JSBW+18, GOC16]. The absence of this signature in the tube suggests that the generation pathway for reactive nitrogen species is closely tied to plasma-liquid interaction processes, likely involving direct reactions between plasma-generated nitrogen and oxygen fragments and water molecules or dissolved gases at the interface [WWF+25].

At position 1, the emission spectrum is dominated by He lines. Pronounced signals of N_2^+ (390 nm and 427 nm) and atomic oxygen O (777 nm and 844 nm) are also present; these are likely due to impurities in the helium gas bottle, as similar emissions were observed in spectra recorded without water in the reactor (not shown in this work). The spectrum also displays noticeable signals from OH(A–X) (282–308 nm) and H_α (656 nm), both of which originate from the dissociation of trace water molecules present in the plasma channel [XZR+25]. At position 2, the emission from OH and H grows markedly, reflecting intensified production of these radicals at the interface—where direct plasma contact with liquid promotes enhanced dissociation and radical formation.

Similar trends were observed for all tested gas mixtures (He–0.2% O_2, He–0.2% N_2, and He–0.2% air): the plasma–liquid region is systematically characterized by enriched NO, OH, and H emissions, underscoring the efficient chemistry enabled by plasma–liquid interaction (not shown).

To investigate the effect of the carrier gas composition on plasma-generated at the plasma-liquid interface, Figure 10 presents a comparative histogram of the integrated intensities of major emission lines and bands detected at position 2. The selected features—NO(A-X)(0-0) (247 nm), OH(A-X)(0-0) (308 nm), N_2(C-B)(0-0) (337 nm), N_2^+(B-X)(0-0) (391nm), H_α (656 nm), He (706 nm), O (777 nm), and O (844nm)—represent the main oxidizing and energetic species involved in plasma-induced aqueous chemistry. The error bars reflect substantial intensity fluctuations, primarily attributable to the dynamic nature of bubble formation and gas flow at the tube outlet, which modulate local plasma stability and optical collection.

NO and H emissions remain relatively unchanged regardless of the carrier gas composition, suggesting that NO formation at the interface is robust across all tested conditions and that its production is governed predominantly by interfacial plasma-liquid interactions (rather than bulk N_2 content), in line with previous reports [ZT23, SMvD+24]. The persistent H_a intensity similarly indicates consistent water dissociation independent of the small variations in gas admixture [TK14].

In contrast, N_2(C-B) and N_2^+(B-X) bands are markedly enhanced for He-0.2% N_2 and He–0.2% air with the strongest emissions for the He-0.2% N_2 mixture. This is expected given the direct supply of molecular nitrogen, and highlights efficient electron-impact excitation and ionization of N_2 under these conditions. The observation that N_2^+ emission is higher for pure He than for He-0.2% O_2 likely arises from residual N_2 impurities in helium and possible quenching by oxygen in the latter mixture [GSL01].

Atomic oxygen (O) emissions at 777 nm and 844 nm are most intense for the He-0.2% O_2 mixture, as O_2 provides a direct source of oxygen atoms through electron-impact dissociation. This confirms that O_2 admixtures effectively boost the yield of reactive atomic oxygen, an important oxydant in plasma-activated solutions [RSS25].

The OH(A–X) emission demonstrates the following trend: He-0.2% N_2 > He ≈ He–0.2% air > He-0.2% O_2. The enhancement in the presence of N_2 may reflect synergistic effects between nitrogen and water vapor at the interface, triggering more efficient production of hydroxyl radicals via excitation transfer or secondary chemistry [WNB25, XZR+25]. The relatively lower OH emission with O_2 may be explained by quenching or competition with O atom formation pathways.

In summary, the data highlight the specific of plasma-liquid interfacial chemistry. The addition of N_2

or air strongly promotes N_2 and N_2^+-related emissions, and maximizes OH formation. The addition of O_2 increases atomic oxygen, but tends to reduce OH intensity, possibly via secondary reactions. NO and H emissions appear insensitive to gas admixture compared to other emissions, emphasizing their formation at the plasma–liquid frontier. These findings underscore the critical influence of minor carrier gas modifications on the generation of short-lived oxidizing and nitrogen species, which directly affect the chemical reactivity of plasma-treated water.

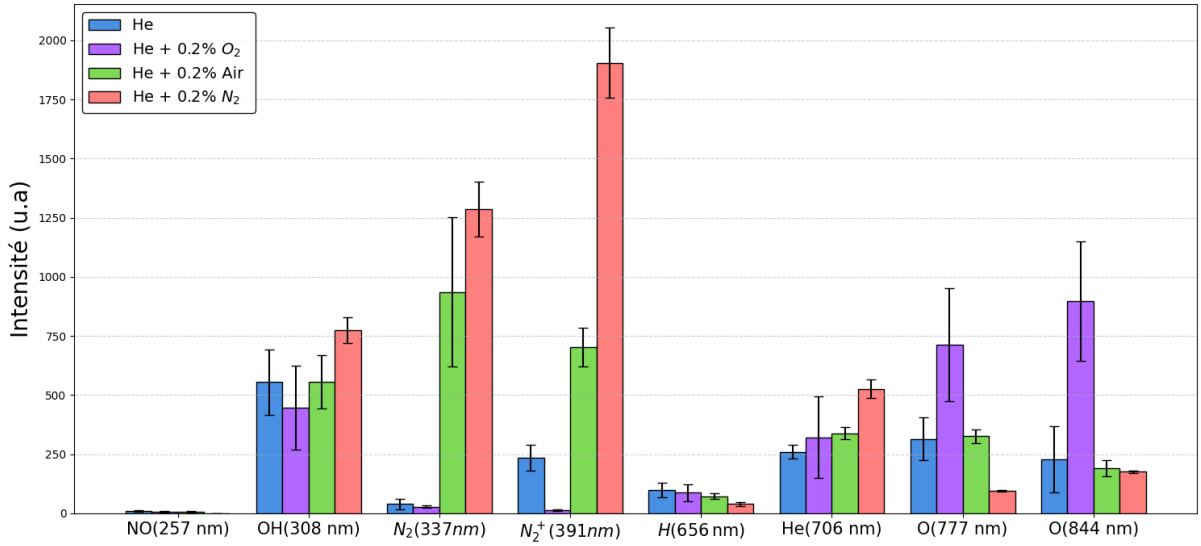

Figure 10: Histogram comparing the intensities of the main spectral features obtained at the plasma-water interface for different carrier gases. The gas flow rate was fixed at 2 L·min^{-1}, with an applied voltage of 15 kV at 20 kHz. The container held 47 mL of ultrapure water.

3.1.3 Reactive species generated in the liquid phase

The chemical composition of the plasma phase, influenced by the carrier gas mixture, determine the nature and quantities of reactive oxygen and nitrogen species (RONS) produced at the plasma-liquid interface and subsequently transferred to the treated water. To quantify this effect, 47mL of ultrapure water was exposed for 15 min to plasma generated using various carrier gas compositions (He, He-0.2% N_2, He-0.2% air, He-0.2% O_2) at 2 L·min^{-1}, 15 kV and 20 kHz. The presence of reactive oxygen species (ROS) in the water were then assessed using the potassium iodide KI-starch method, with absorbance at 600 nm serving as proxy for overall oxidant formation (see Figure 11).

The measured absorbance follows the trend:

$$\text{He + 0.2\% } N_2 > \text{He + 0.2\% air} > \text{He} > \text{He + 0.2\% } O_2.$$

The reactive oxygen species (ROS) created in water originate from the dissociation of water molecules and, when O_2 is present, from the dissociation of O_2 at the water–plasma interface. When Helium is used as the carrier gas, ROS—such as OH and H_2O_2—primarily originate via direct electron impact dissociation of water molecule at the plasma-liquid interface, a mechanism well documented in the literature [WNB25]:

$$e^- + H_2O \rightarrow H + OH + e^- \tag{10}$$

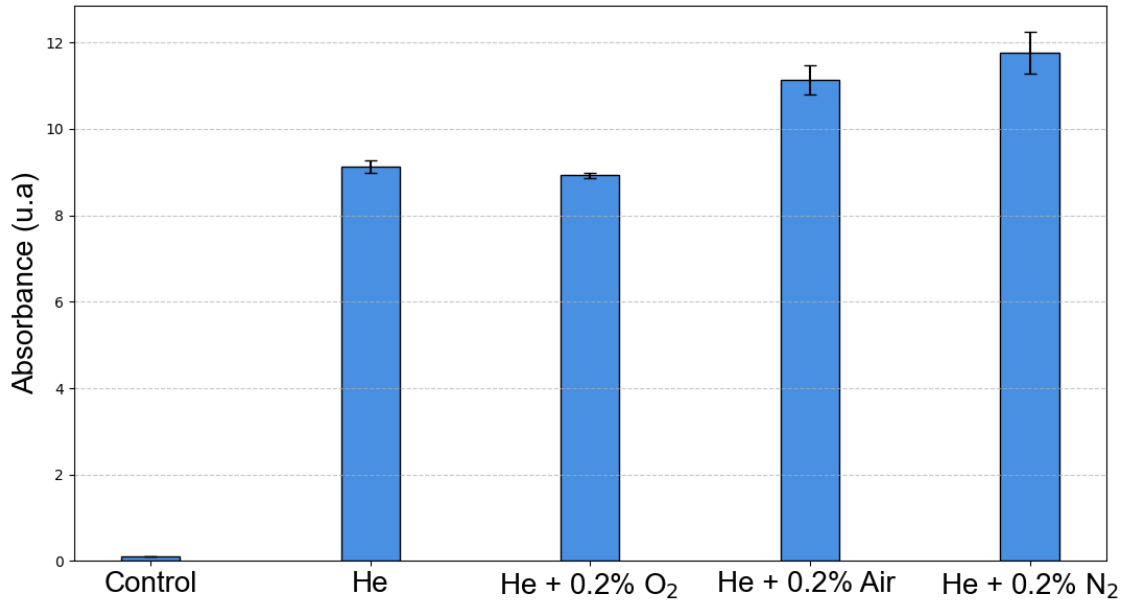

Figure 11: Absorbance at 600 nm of the mixture of KI–starch solution and plasma-treated water. A total of 47 mL of ultrapure water was treated for 15 min using a plasma device with a gas flow rate of 2 L·min^{-1}, an applied voltage of 15 kV, and an operating frequency of 20 kHz. The control sample was prepared by purging ultrapure water with helium flowing at 2 L·min^{-1} for 15 min without plasma discharge.

$$OH + OH \rightarrow H_2O_2 \tag{11}$$

Addind a small fraction of nitrogen (He-0.2% N_2) or air to the carrier gas increases the ROS concentration in the liquid. This enhancement is attributed to the formation of excited N_2 molecules by electron impact in the plasma, which can subsequently transfer their energy efficiently to water molecules, promoting OH and H production via secondary reactions [UKBC18, Uhm15]. In OES measurements (Figure 10), this effect is directly evidenced by the growth of N_2(C-V) and N_2^+(B-X) emissions for these mixtures.

$$e^- + N_2 \rightarrow N_2^* + e^- \tag{12}$$

$$N_2^* + H_2O \rightarrow N_2 + OH + H \tag{13}$$

Somewhat counterintuitively, the introduction of O_2 (He-0.2% O_2) does not increase but rather decreases the final ROS content. A plausible explanation is that the electronegativity of O_2 which is known to efficiently capture plasma electrons, may lead to a reduction in the overall electron density and therefore reduce the efficiency of both direct water dissociation and the secondary energy transfer from excited species [ZWW18]. Additionally, the presence of O_2 promotes quenching processes, in particular the rapid removal of excited N_2^* according to reaction below, which both decreases the available N_2^* for water activation and increases O atoms in the plasma [BKC11, GETN$^+$23]. This interpretation is consistent with the observed OES trends and KI–starch measurements, although direct electron-density diagnostics would be required to confirm it quantitatively. It also provides a plausible explanation for the lower N_2 emission intensity (see Figure 10) and the reduced ROS yield detected in the plasma-treated water for O_2-containing mixtures (see Figure 11).

$$N_2^* + O_2 \rightarrow 2\,O + N_2 \tag{14}$$

In summary, the experimental data and their interpretation are in excellent agreement with current plasma–liquid literature: the presence of N_2 (pure or in air) in the carrier gas introduces additional energy transfer channels that synergistically boost ROS formation [ZT23, Uhm15], whereas O_2 tends to reduce overall ROS yields via electron scavenging and quenching of energetic intermediates [MIA+24, MLK20].

4 Conclusion

This study demonstrates the potential of an immersed dielectric barrier discharge (DBD) plasma source for the generation of reactive oxygen and nitrogen species (RONS) and the chemical modification of water at the plasma-liquid interface. Through a comprehensive suite of electrical, optical, and chemical diagnostics, we systematically characterized the discharge behavior, energy coupling, spatiotemporal propagation, and species formation under varying carrier gas compositions. Detailed optical emission spectroscopy revealed that plasma-liquid interactions uniquely favor the generation of short-lived reactive species, such as OH, O, NO, and H, with their yields strongly modulated by the gas-phase composition and the nature of the plasma-liquid interaction.

Key findings include the strong enhancement of OH and N_2/N_2^+ emissions in the presence of nitrogen, and the increased of atomic oxygen with O_2 admixture—each reflecting distinct underlaying reaction pathways. Chemical analysis using the KI-starch method confirmed that the oxidant yield in plasma-treated water is maximized with small additions of N_2 or air to the helium carrier. In contrast, introducing O_2, despite providing a direct source of atomic oxygen, leads to a decrease in overall ROS content, as a result of electron attachment and quenching of excited nitrogen species—emphasizing the balance required between plasma reactivity and gas composition.

In the present work, all electrical measurements were performed at the beginning of plasma operation, when the conductivity of the ultrapure water remains very low and the liquid can be reasonably treated as a dielectric layer in the equivalent-circuit model. As plasma exposure progresses, the accumulation of plasma-generated species is expected to increase the liquid conductivity and, in turn, to modify the discharge regime and the way energy is coupled into the plasma. A detailed investigation of how the energy dissipated in the discharge evolves as a function of the water conductivity—by combining time-resolved electrical diagnostics with *in situ* conductivity monitoring—thus constitutes an important perspective for future work.

While these insights provide a useful basis for optimizing plasma water treatment in our experimental conditions, further studies are also needed to comprehensively quantify the main oxidizing and nitrogenous species (O_3, OH, H_2O_2, NO_2^-, NO_3^-) in solution under realistic conditions, and to correlate their formation with the plasma's physicochemical environment and intended decontamination targets. Such future investigations will be essential to refine mechanistic understanding and guide the practical implementation of DBD plasma technologies for local and decentralized water treatment applications.

References

[BKK+21] G. T. Bae, J. Y. Kim, D. Y. Kim, E. Y. Jung, H. J. Jang, C.-S. Park, H. Jang, D. H. Lee, H.-K. Lee, and H.-S. Tae, Potential application of pin-to-liquid dielectric barrier discharge structure in decomposing aqueous phosphorus compounds for monitoring water quality, *Materials* **14** no. 24 (2021), 7559. doi:10.3390/ma14247559.

[BKC11] M. S. Bak, W. Kim, and M. A. Cappelli, On the quenching of excited electronic states of molecular nitrogen in nanosecond pulsed discharges in atmospheric pressure air, *Applied Physics Letters* **98** no. 1 (2011), 011502. doi:10.1063/1.3535986.

[BLU+22] D. Boonyawan, K. Lamasai, C. Umongno, S. Rattanatabtimtong, L. Yu, C. Kuensaen, J. Maitip, and P. Thana, Surface dielectric barrier discharge plasma–treated pork cut parts: bactericidal efficacy and physiochemical characteristics, *Heliyon* **8** no. 10 (2022), e10915. doi:10.1016/j.heliyon.2022.e10915.

[BKL+16] P. J. Bruggeman, M. J. Kushner, B. R. Locke, J. G. Gardeniers, W. Graham, D. B. Graves, R. Hofman-Caris, D. Maric, J. P. Reid, E. Ceriani, and others, Plasma–liquid interactions: a review and roadmap, *Plasma sources science and technology* **25** no. 5 (2016), 053002. doi:10.1088/0963-0252/25/5/053002.

[CAB+17] A. Christou, A. Agüera, J. M. Bayona, E. Cytryn, V. Fotopoulos, D. Lambropoulou, C. M. Manaia, C. Michael, M. Revitt, P. Schröder, and others, The potential implications of reclaimed wastewater reuse for irrigation on the agricultural environment: the knowns and unknowns of the fate of antibiotics and antibiotic resistant bacteria and resistance genes–a review, *Water research* **123** (2017), 448–467. doi:10.1016/j.watres.2017.07.004.

[CER99] P. Colpo, R. Ernst, and F. Rossi, Determination of the equivalent circuit of inductively coupled plasma sources, *Journal of applied physics* **85** no. 3 (1999), 1366–1371. doi:10.1063/1.369268.

[CMM+21] I. Courti, C. Muja, T. Maho, F. P. Sainct, and P. Guillot, Impact of bacterial growth phase on liquid decontamination efficiency using atmospheric pressure plasma, *Plasma Medicine* **11** no. 4 (2021), 85–104. doi:10.1615/PlasmaMed.2022041486.

[CMM+22] I. Courti, C. Muja, T. Maho, F. P. Sainct, and P. Guillot, Degradation of bacterial antibiotic resistance genes during exposure to non-thermal atmospheric pressure plasma, *Antibiotics* **11** no. 6 (2022), 747. doi:10.3390/antibiotics11060747.

[GETN+23] R. Ghobeira, P. S. Esbah Tabaei, A. Nikiforov, R. Morent, and N. De Geyter, Unraveling exclusive in-plasma initiated oxidation processes occurring at polymeric surfaces upon O2 admixtures to medium pressure ar and N2 DBD treatments, *Polymers* **15** no. 14 (2023), 2978. doi:10.3390/polym15142978.

[GOC16] Y. Gorbanev, D. O'Connell, and V. Chechik, Non-thermal plasma in contact with water: the origin of species, *Chemistry–A European Journal* **22** no. 10 (2016), 3496–3505. doi:10.1002/chem.201503771.

[GSL01] V. Guerra, P. Sa, and J. Loureiro, Role played by the N2 (A3Σu+) metastable in stationary N2 and N2-O2 discharges, *Journal of Physics D: Applied Physics* **34** no. 12 (2001), 1745. doi:10.1088/0022-3727/34/12/301.

[GBB+21] P. Gururani, P. Bhatnagar, B. Bisht, V. Kumar, N. C. Joshi, M. S. Tomar, and B. Pathak, Cold plasma technology: advanced and sustainable approach for wastewater treatment, *Environmental Science and Pollution Research* **28** no. 46 (2021), 65062–65082. doi:10.1007/s11356-021-16741-x.

[JSBW+18] H. Jablonowski, A. Schmidt-Bleker, K.-D. Weltmann, T. Von Woedtke, and K. Wende, Non-touching plasma–liquid interaction–where is aqueous nitric oxide generated?, *Physical Chemistry Chemical Physics* **20** no. 39 (2018), 25387–25398. doi:10.1039/C8CP02412J.

[LLKA04] M. Laroussi, X. Lu, V. Kolobov, and R. Arslanbekov, Power consideration in the pulsed dielectric barrier discharge at atmospheric pressure, *Journal of Applied Physics* **96** no. 5 (2004), 3028–3030. doi:10.1063/1.1777392.

[LMZ+19] J. Li, C. Ma, S. Zhu, F. Yu, B. Dai, and D. Yang, A review of recent advances of dielectric barrier discharge plasma in catalysis, *Nanomaterials* **9** no. 10 (2019), 1428. doi:10.3390/nano9101428.

[LN01] S. Liu and M. Neiger, Excitation of dielectric barrier discharges by unipolar submicrosecond square pulses, *Journal of Physics D: Applied Physics* **34** no. 11 (2001), 1632. doi:10.1088/0022-3727/34/11/312.

[LN03] S. Liu and M. Neiger, Electrical modelling of homogeneous dielectric barrier discharges under an arbitrary excitation voltage, *Journal of Physics D: Applied Physics* **36** no. 24 (2003), 3144. doi:10.1088/0022-3727/36/24/009.

[LWZ+22] X. Lu, S. Wang, R. Zhou, Z. Fang, and P. Cullen, Discharge modes and liquid interactions for plasma-bubble discharges, *Journal of Applied Physics* **132** no. 7 (2022), 073303. doi:10.1063/5.0094560.

[MIA+24] M. Majeed, M. Iqbal, M. Altin, Y.-N. Kim, D. K. Dinh, C. Lee, Z. Ali, and D. H. Lee, Effect of thermal gas quenching on NOx production by atmospheric pressure rotating arc plasma: A pathway towards eco-friendly fertilizer, *Chemical Engineering Journal* **485** (2024), 149727. doi:10.1016/j.cej.2024.149727.

[MKNK20] F. Mitsugi, S. Kusumegi, K. Nishida, and T. Kawasaki, Visualization of plasma-induced liquid flow using KI–starch and PIV, *IEEE Transactions on Plasma Science* **49** no. 1 (2020), 9–14. doi:10.1109/TPS.2020.2986775.

[MLK20] S. Mohades, A. M. Lietz, and M. J. Kushner, Generation of reactive species in water film dielectric barrier discharges sustained in argon, helium, air, oxygen and nitrogen, *Journal of Physics D: Applied Physics* **53** no. 43 (2020), 435206. doi:10.1088/1361-6463/aba21a.

[NMMR+25] Y. Nahum, J. Muhvich, J. R. Morones-Ramirez, N. G. Casillas-Vega, and M. H. Zaman, Biofilms as potential reservoirs of antimicrobial resistance in vulnerable settings, *Frontiers in Public Health* **13** (2025), 1568463. doi:10.3389/fpubh.2025.1568463.

[PGK+11] U. N. Pal, P. Gulati, N. Kumar, M. Kumar, M. Tyagi, B. Meena, A. Sharma, and R. Prakash, Analysis of discharge parameters in xenon-filled coaxial DBD tube, *IEEE Transactions on Plasma Science* **39** no. 6 (2011), 1475–1481. doi:10.1109/TPS.2011.2142197.

[PZDdlSBC+17] O. A. Palacios, F. J. Zavala-Diaz de la Serna, M. d. L. Ballinas-Casarrubias, M. S. Espino-Valdés, and G. V. Nevárez-Moorillón, Microbiological impact of the use of reclaimed wastewater in recreational parks, *International journal of environmental research and public health* **14** no. 9 (2017), 1009. doi:10.3390/ijerph14091009.

[PB19] A. V. Pipa and R. Brandenburg, The equivalent circuit approach for the electrical diagnostics of dielectric barrier discharges: The classical theory and recent developments, *Atoms* **7** no. 1 (2019), 14. doi:10.3390/atoms7010014.

[PHK+12] A. Pipa, T. Hoder, J. Koskulics, M. Schmidt, and R. Brandenburg, Experimental determination of dielectric barrier discharge capacitance, *Review of Scientific Instruments* **83** no. 7 (2012), 075111. doi:10.1063/1.4737623.

[PKBH12] A. Pipa, J. Koskulics, R. Brandenburg, and T. Hoder, The simplest equivalent circuit of a pulsed dielectric barrier discharge and the determination of the gas gap charge transfer, *Review of Scientific Instruments* **83** no. 11 (2012), 115112. doi:10.1063/1.4767637.

[RHZ+23] C. Ren, B. Huang, C. Zhang, B. Qi, W. Chen, and T. Shao, Impact of surface charges on energy deposition in surface dielectric barrier discharge: a modeling investigation, *Plasma Sources Science and Technology* **32** no. 2 (2023), 025004. doi:10.1088/1361-6595/acb4b9.

[RSS25] C. D. Robinson, N. L. Sponsel, and K. Stapelmann, Bubbling water-treating DBD plasma device optimization using experimental and computational methods, *Plasma Processes and Polymers* **22** no. 5 (2025), 70000. doi:10.1002/ppap.70000.

[SGA+20] K. Saber, H. Guedah, A. Abahazem, N. Merbahi, and M. Yousfi, Electrical equivalent circuit and modeling of a pulsed air corona discharge, *Materials Today: Proceedings* **24** (2020), 119–124. doi:10.1016/j.matpr.2019.07.703.

[SN23] S. S. Sambaza and N. Naicker, Contribution of wastewater to antimicrobial resistance: A review article, *Journal of global antimicrobial resistance* **34** (2023), 23–29. doi:10.1016/j.jgar.2023.05.010.

[SMvD+24] M. Shaban, N. Merkert, A. C. van Duin, D. van Duin, and A. P. Weber, Advancing DBD plasma chemistry: insights into reactive nitrogen species such as NO2, N2O5, and N2O optimization and species reactivity through experiments and MD simulations, *Environmental Science & Technology* **58** no. 36 (2024), 16087–16099. doi:10.1021/acs.est.4c04894.

[SSK23] H. Shi, K. Shen, and T. Kawasaki, Effect of supplied gas on ROS transport through liquid targets by plasma jet irradiation, *Int. J. Plasma Environ. Sci. Technol* **17** no. 1 (2023), e01003. doi:10.34343/ijpest.2023.17.e01003.

[SW21] E. Slikboer and J. Walsh, Impact of electrical grounding conditions on plasma–liquid interactions using Thomson scattering on a pulsed argon jet, *Scientific reports* **11** (2021), 17749. doi:10.1038/s41598-021-97185-8.

[SFBK11] B. S. Sommers, J. E. Foster, N. Y. Babaeva, and M. J. Kushner, Observations of electric discharge streamer propagation and capillary oscillations on the surface of air bubbles in water, *Journal of Physics D: Applied Physics* **44** no. 8 (2011), 082001. doi:10.1088/0022-3727/44/8/082001.

[SSSM22] T. Stachurová, N. Sýkorová, J. Semerád, and K. Malachová, Resistant genes and multidrug-resistant bacteria in wastewater: A study of their transfer to the water reservoir in the czech republic, *Life* **12** no. 2 (2022), 147. doi:10.3390/life12020147.

[TK14] W. Tian and M. J. Kushner, Atmospheric pressure dielectric barrier discharges interacting with liquid covered tissue, *Journal of Physics D: Applied Physics* **47** no. 16 (2014), 165201. doi:10.1088/0022-3727/47/16/165201.

[TSC+23] G. Tomei, M. Saleem, E. Ceriani, A. Pinton, E. Marotta, and C. Paradisi, Cold plasma for green advanced reduction/oxidation processes (arops) of organic pollutants in water, *Chemistry–A European Journal* **29** no. 65 (2023), e202302090. doi:10.1002/chem.202302090.

[TBB24] V. Trotta, O. Baaloudj, and M. Brienza, Risks associated with wastewater reuse in agriculture: investigating the effects of contaminants in soil, plants, and insects, *Frontiers in Environmental Science* **12** (2024), 1358842. doi:10.3389/fenvs.2024.1358842.

[Uhm15] H. S. Uhm, Generation of various radicals in nitrogen plasma and their behavior in media, *Physics of Plasmas* **22** no. 12 (2015), 123506. doi:10.1063/1.4936796.

[UKBC18] H. S. Uhm, S. H. Ki, K. Y. Baik, and E. H. Choi, Influence of oxygen on generation of reactive chemicals from nitrogen plasma jet, *Scientific Reports* **8** (2018), 9318. doi:10.1038/s41598-018-27473-3.

[VNBL18] P. Vanraes, A. Nikiforov, A. Bogaerts, and C. Leys, Study of an AC dielectric barrier single micro-discharge filament over a water film, *Scientific reports* **8** (2018), 10919. doi:10.1038/s41598-018-29189-w.

[VNL16] P. Vanraes, A. Y. Nikiforov, and C. Leys, Electrical discharge in water treatment technology for micropollutant decomposition, in *Plasma Science and Technology - Progress in Physical States and Chemical Reactions* (T. Mieno, ed.), IntechOpen, London, 2016. doi:10.5772/61830.

[WNB25] J. Wang, G. Nayak, and P. J. Bruggeman, OH density and water vapor concentration gradients during plasma-droplet interactions, *Frontiers in Physics* **13** (2025), 1592169. doi:10.3389/fphy.2025.1592169.

[WWF+25] J. Wang, M. Wang, J. Fang, S. Xu, Y. Guo, K. Ding, and J. Shi, Plasma-activated water: Effects of gas–liquid interface interaction and discharge intensity on activation properties, *Physics of Plasmas* **32** no. 3 (2025), 033505. doi:10.1063/5.0239515.

[XZR+25] W. Xi, H. Zhang, W. Ren, J. Li, N. Chen, M. Chen, W. Han, and C. Cheng, Mechanisms of OH and H2O2 formation in the liquid phase induced by an atmospheric pressure plasma jet with oxygen introduction, *Physics of Plasmas* **32** no. 8 (2025), 083505. doi:10.1063/5.0268974.

[YJY+18] S.-Y. Yoon, H. Jeon, C. Yi, S. Park, S. Ryu, and S. B. Kim, Mutual interaction between plasma characteristics and liquid properties in AC-driven pin-to-liquid discharge, *Scientific reports* **8** (2018), 12037. doi:10.1038/s41598-018-30540-4.

[ZNTK+20] H. Zeghioud, P. Nguyen-Tri, L. Khezami, A. Amrane, and A. A. Assadi, Review on discharge plasma for water treatment: Mechanism, reactor geometries, active species and combined processes, *Journal of Water Process Engineering* **38** (2020), 101664. doi:10.1016/j.jwpe.2020.101664.

[ZYW+19] L. Zhang, D. Yang, S. Wang, Z. Jia, H. Yuan, Z. Zhao, and W. Wang, Discharge regimes transition and characteristics evolution of nanosecond pulsed dielectric barrier discharge, *Nanomaterials* **9** no. 10 (2019), 1381. doi:10.3390/nano9101381.

[ZT23] X. Zhao and Y. Tian, Sustainable nitrogen fixation by plasma-liquid interactions, *Cell Reports Physical Science* **4** no. 10 (2023), 101618. doi:10.1016/j.xcrp.2023.101618.

[ZWW18] Y. Zheng, L. Wang, and D. Wang, Effect of oxygen as additive on an atmospheric nanosecond pulsed helium plasma jet impinging on a dielectric surface, *Journal of Applied Physics* **124** no. 12 (2018), 123301. doi:10.1063/1.5036668.